remote sensing

*Technical Note*

# Identifying Potential Landslides on Giant Niexia Slope (China) Based on Integrated Multi-Remote Sensing Technologies

**Xiujun Dong [1], Tao Yin [2], Keren Dai [1,2,3,4,*], Saied Pirasteh [5,6], Guanchen Zhuo [1,2], Zhiyu Li [2], Bing Yu [7] and Qiang Xu [1]**

1 State Key Laboratory of Geological Disaster Prevention and Geological Environmental Protection, Chengdu University of Technology, Chengdu 610059, China
2 College of Earth Science, Chengdu University of Technology, Chengdu 610059, China
3 Key Laboratory of Earth Exploration and Information Techniques, Chengdu University of Technology, Ministry of Education, Chengdu 610059, China
4 The College of Geological Engineering and Geomatics, Chang'an University, Xi'an 710064, China
5 GeoAI, Smarter Map and LiDAR Lab, Faculty of Geosciences and Environmental Engineering, Southwest Jiaotong University, Chengdu 610097, China
6 Department of Geotechnics and Geomatics, Saveetha School of Engineering, Saveetha Institute of Medical and Technical Sciences, Chennai 602105, India
7 School of Civil Engineering and Geomatics, Southwest Petroleum University, Chengdu 610500, China
* Correspondence: daikeren17@cdut.edu.cn

**Abstract:** The Niexia slope, located in Danba County, Sichuan Province, China, with steep slope terrain and dense vegetation coverage, has a height difference of about 3002 m. A traditional manual survey cannot be performed here, and single remote sensing technology is not comprehensive enough to identify potential landslides on such high and steep slopes. In this paper, an integrated approach with multi-remote sensing techniques was proposed to identify potential landslides of the Niexia slope, which combined Interferometry Synthetic Aperture Radar (InSAR), airborne Light Detection and Ranging (LiDAR), and optical remote sensing technologies. InSAR technology was used to monitor the small displacements of the whole slope, and three potential landslides on Niexia slope were identified. The maximum cumulative displacement reached up to 11.9 cm over 1 year. Subsequently, high-resolution optical remote sensing images acquired by remote sensing satellites and a Digital Elevation Model (DEM) without vegetation influence obtained by LiDAR were used to finely interpret the sign of landslide micro-geomorphology and to determine the potential landslide geometry boundaries. As a result, four and nine potential landslides with landslide micro-geomorphic features were identified, respectively. Finally, the identification results of the three techniques were fused and analyzed to assess the potential landslides on the Niexia slope. We compared the results from multi-remote sensing technologies, showing that the three techniques have advantages and disadvantages in terms of monitoring objects, monitoring range, and monitoring accuracy. The integrated use of these three technologies can identify and monitor potential landslides more comprehensively, which could play an important role in the future.

**Keywords:** interferometric synthetic aperture radar (InSAR); airborne light detection and ranging (LiDAR) technology; optical remote sensing; Niexia slope

check for updates

**Citation:** Dong, X.; Yin, T.; Dai, K.; Pirasteh, S.; Zhuo, G.; Li, Z.; Yu, B.; Xu, Q. Identifying Potential Landslides on Giant Niexia Slope (China) Based on Integrated Multi-Remote Sensing Technologies. *Remote Sens.* **2022**, *14*, 6328. https://doi.org/10.3390/rs14246328

Academic Editors: Alberto Moreira, Mihai Datcu, Chao Wang, Fan Wu and Ruya Xiao

Received: 27 October 2022
Accepted: 6 December 2022
Published: 14 December 2022



## 1. Introduction

The data show that between 2004 and 2010, there were a total of 2620 fatal landslides, resulting in a record 32,322 deaths and between January 2004 and December 2016, and a total of 55,997 people lost their lives in 4862 different landslides [1,2]. High mountain and valley areas cause a large number of landslides due to their complex topographic conditions. For example, the landslide in the Pink Mountains of Canada in 2002 had a height difference of about 3002 m and a movement distance of about 2 km [3]. The landslide in Xinmo Village in 2017 caused a 2 km blockage of the river and buried more than 100 people [4]. The Anangzhai ancient landslide occurred on 17 June 2020, causing a weir, leaving 15 people stranded and 1 person lost [5]. The Tupul landslide in Manipur, India, in June 2022, wiped out the under-construction Tupul railway station and caused the loss of more than 54 lives [6]. These slopes are located in areas with steep slope terrain, dense vegetation coverage, and a large height difference. Simultaneously, the disasters are sudden, highly destructive, and strongly concealed, posing a severe threat to the safety of local residents and causing huge losses to economic properties. Therefore, comprehensively identifying and monitoring potential landslides on high and steep slopes is of great importance.

Remote sensing technology can overcome the problem that traditional survey methods cannot identify potential landslides in high mountain valley areas. Niexia slope, with steep slope terrain and dense vegetation coverage, has a height difference of about 3002 m. In recent years, the usage of remote sensing technology for landslide identification and monitoring has been increasing [7,8]. Among them, InSAR technology, which can conduct displacement identification over a wide area with high accuracy and is not affected by weather conditions, is applied by many researchers for the identification of the early stage of potential landslides [9–20]. With a good vegetation penetration ability, the LiDAR technology can obtain DEM with geomorphic features, which has also gradually been applied in landslide identification and boundary determination [21–32]. In real-time, the high-resolution optical images that are acquired by remote sensing satellites can well reflect the geomorphological characteristics of landslides and become an important tool for researchers to identify landslide boundaries and conduct the spatial and temporal evolution analysis of landslides [3,33–42]. For the Jiaju landslide, which is located on the Niexia slope, a number of scholars have also conducted related studies; for example, Yin et al. (2010) combined GPS and InSAR techniques to monitor the vertical and horizontal slip rates in its northern and southern regions [43]; Dong et al. (2008) identified its surface displacement based on the improved coherent scatterer InSAR (CSI) technique [44]; and Ao et al. (2019) combined geological data and SAR images to reconstruct 3D displacement fields to identify their 3D displacement processes [45]. The above three studies show that the displacement rate in the northern region was greater than that in the southern region in the Jiaju landslide. The aforementioned literature review shows three remote sensing techniques that have advantages and disadvantages. InSAR technology can identify small displacements. LiDAR technology and optical remote sensing can represent the landslide landscape. LiDAR technology can remove the influence of vegetation. However, a single remote sensing technique is not comprehensive enough to identify potential landslides on high and steep slopes in mountainous areas [46,47] The integration of the three techniques to evaluate potential landslides on high and steep slopes deserves further research.

This paper proposes an integrated approach with multi-remote sensing techniques to identify potential landslides of the giant Niexia slope. InSAR technology was used to monitor small displacements of the slope, and the optical remote sensing image and LiDAR technique were based on micro-geomorphology for the fine interpretation of potential landslide boundaries. LiDAR technology removes the influence of vegetation. The combined use of the three techniques can more comprehensively identify and monitor potential landslides on high and steep slopes.

## 2. Study Area and Datasets

### 2.1. Study Area

The study area is located in Danba County, in the southwestern part of Sichuan Province, China (Figure 1a). Danba County is a typical alpine valley landscape adjacent to Jinchuan County, Daofu County, and other counties. As shown in Figure 1, the blue dashed box is the coverage area of SAR images (Figure 1b). The study area, about 14 km from Danba County, is mainly the Niexia slope located in the upper part of the Dajinchuan River, with dense vegetation cover inside the area and erosion of the slope toe by the Dajinchuan River (Figure 1c). The lowest elevation of the Niexia slope is 1897 m, and the highest elevation reaches 4593 m (Figure 1d). This region belongs to the Tibetan plateau-type monsoon climate, the annual precipitation is 600 mm, and the sunshine is sufficient. The complex geographical environment and climatic conditions make the study area a geohazard-prone area [48].

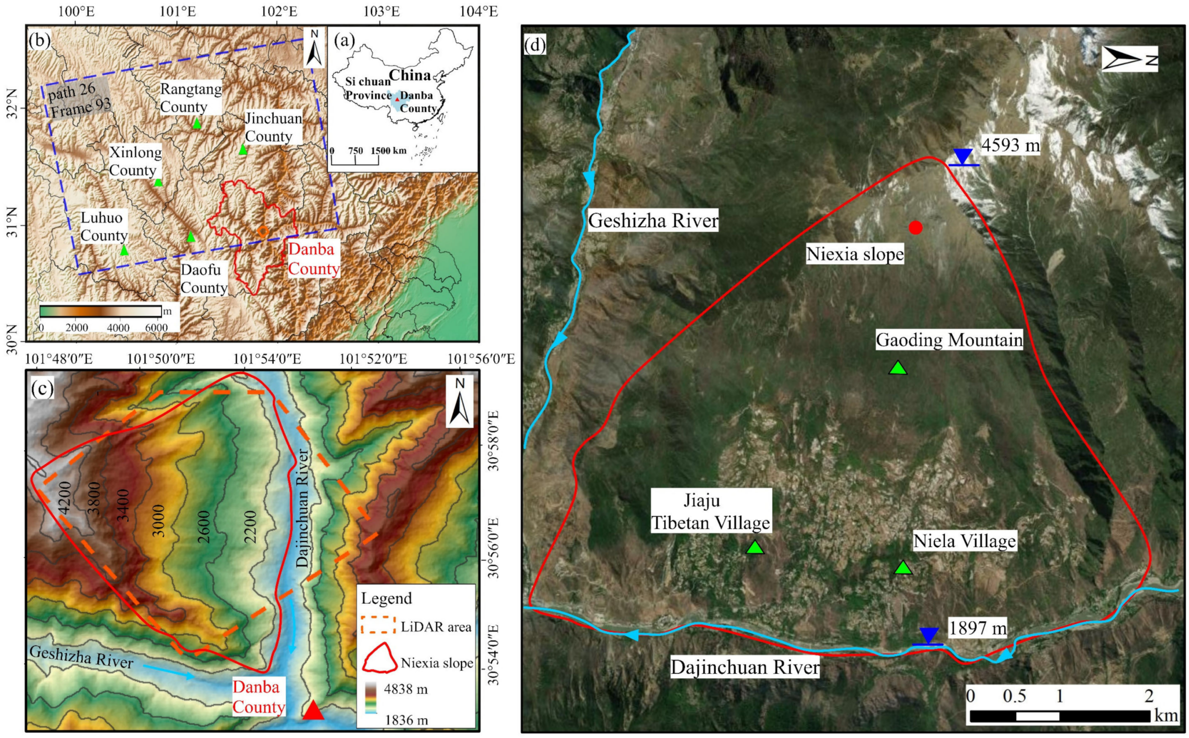


**Figure 1.** (**a**) Danba County basic location; (**b**) SAR image coverage and basic location of the study area; (**c**) optical image covering the study area; (**d**) topographic and elevation information of the study area.

## *2.2. Datasets*

Sentinel-1, an earth observation satellite launched by the European Space Agency (ESA) in 2014, is carrying C-band with a revisit cycle of 12 days. Twenty-nine Sentinel-1 ascending images from 26 February 2020 to 8 February 2021 were acquired covering the study area. The main parameters are shown in Table 1. The DEM used is the Shuttle Radar Topography Mission (SRTM) data with 30 m spatial resolution, which is mainly measured jointly by the National Aeronautics and Space Administration (NASA) and the National Imagery and Mapping Agency (NIMA) [49].

**Table 1.** Satellite data main parameters.

| Parameter | Description |
|---|---|
| Orbit direction | Ascending |
| Temporal coverage | 26 February 2020–8 February 2021 |
| Wavelength | 5.6 cm |
| Polarization | VV |
| Azimuth/Range pixel spacing | 13.99 m/2.33 m |
| Number of images | 29 |
| Incidence/Azimuth angle | 39.27/90 degree |

LiDAR technology with a good vegetation penetration ability can obtain DEM with real micro-landscape features. The LiDAR point cloud data used in this study were acquired in 2018 with a resolution of 0.5 m. First, the ground point data are generated by filtering the obtained point cloud data, and then the DEM is obtained by spatial interpolation. Finally, the obtained DEM data are imported into SAGA software for processing to obtain the Sky View Factor (SVF) [50], as it is more effective in showing the historical displacement area and identifying slope top scars and tension cracks compared with hillshade maps [51].

The optical remote sensing image used for the study was acquired by the Planet Scope Scene satellite on 22 December 2021 with a resolution of 3 m (Planet Scope Scene satellite is free for optical images with a resolution of 3 m and below). This time has less vegetation cover and no cloud cover, which facilitates the visual interpretation based on landslide micro-geomorphology.

## 3. Methodology

In this paper, an integrated multi-remote sensing technologies approach was proposed to identify the potential landslides on the giant Niexia slope. The technical flowchart of the approach is presented in Figure 2, the main steps are as follows:

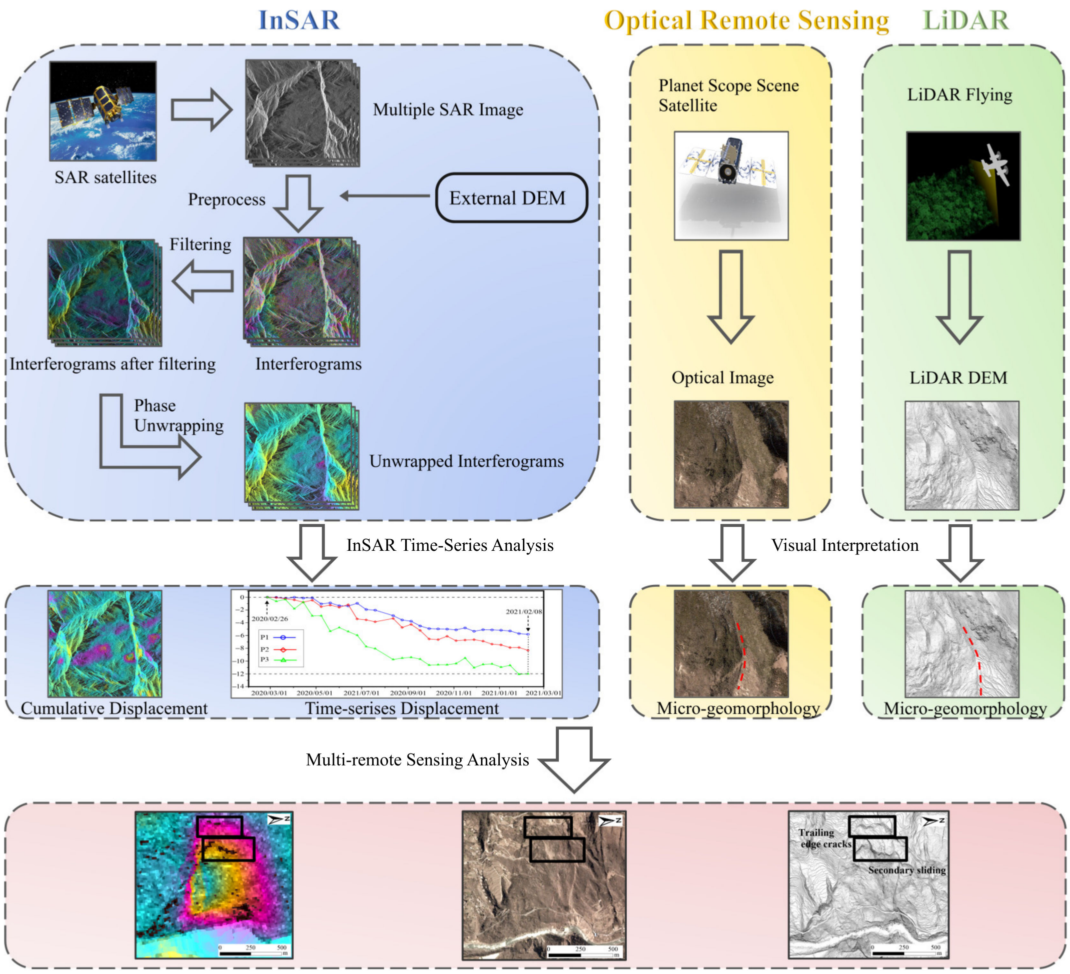


**Figure 2.** The technical flowchart of the integrated multi-remote sensing technologies approach.

The Stacking-InSAR method was used to perform the time series InSAR analysis. Multiple SAR images were acquired by SAR satellites, and interferograms were generated by preprocessing based on multiple SAR images and external DEM, the threshold on perpendicular is 180 m and the temporal baseline is 30 days. Filtering and phase unwrapping were performed to improve the signal to noise ratio of the interferograms and to calculate unwrapped phase signal. By the above processing, unwrapped interferograms were obtained [52–57]. The cumulative displacement were achieved by stacking [58] processing in the GAMMA software.

Second, for optical remote sensing technology, the optical remote sensing images were acquired by the Planet Scope Scene satellite. This technology was used to interpret potential landslides boundary based on landslide micro-geomorphology [3,59].

Third, for LiDAR technology, the point cloud data were acquired by LiDAR flight, then processed to obtain a high-resolution DEM with micro-geomorphic features. This technology was used to finely interpret the sign of landslide micro-geomorphology and to determine the potential landslide geometry boundaries [21,25,60]. LiDAR technology can remove the influence of vegetation.

Finally, we combined the recognition results of the three techniques for analysis. Through multi-source remote sensing analysis (InSAR technology, optical remote sensing, LiDAR technology), we found that each of the three remote sensing techniques has its own advantages and disadvantages for monitoring objects, monitoring range, and monitoring accuracy, and these are applicable to different situations (InSAR technology for the ongoing displacement area; optical remote sensing for the ongoing displacement area and the historical displacement area; LiDAR technology for the historical displacement area).

## 4. Results

Figure 3 shows the time series displacement results of the study area in the past year obtained by the Stacking-InSAR technique. This technique can make the displacement interferograms more continuous in time and space [61,62], and has better performance in low-coherence areas [63]. We identified three potential landslides with significant displacement on the Niexia slope by Stacking-InSAR technique. Among them, Zone I, located on the lower left side of the slope is about 900 km$^2$, with the height difference being about 618 m. Zone II is the potential landslide with the largest displacement range, located in the middle and upper part of the slope, with an area of about 7700 km$^2$, and the height difference is about 1666 m. The potential landslide Zone III is the most significant displacement of the potential landslide, located on the lower right side of the slope, with an area of about 1100 km$^2$, and the height difference is about 507 m. In addition, P1, P2, and P3 were selected for time series displacement analysis on the three potential landslides of Zones I, II, and III, respectively (Figure 3b). The cumulative displacement at points P1, P2, and P3 are 5.8 cm, 8.3 cm, and 11.9 cm, respectively. The displacement characteristics are presented as follows: from 26 February 2020 to 1 May 2020, the displacement of landslides was slow, and it started to increase from 1 May 2020 to 1 October 2020; the displacement gradually levelled off from 1 October 2020 to 8 February 2021, and cumulative displacement reached the maximum on 8 February 2021.

High-resolution optical remote sensing images can clearly represent landslide micro-geomorphology, such as landslide fractures. As for some areas that have experienced historical displacement damage, we can perform potential landslide boundary interpretation based on the landslide back wall, shear cracks on both sides, landslide sidewalls, landslide terraces, and closed depressions [3,59]. In this study, Planet Scope Scene optical remote sensing image with a resolution of 3 m covering the study area dated 22 December 2021 is used, and the potential landslide boundary is decoded for the study area based on the above landslide micro-geomorphic features. The recognition results are shown in Figure 4, a total of four landslides with distinct landslide geomorphic features were identified, and some of these landslides' micro-geomorphology are shown in detail. The detailed view of all zones shows that landslide shear cracks can obviously be seen. Moreover, there is an obvious landslide back wall and landslide sidewalls left after the collapse of historical landslides in zone a2 and a3. Besides, there is a clear difference between the soil quality in the a2 zone and the surrounding soil quality.

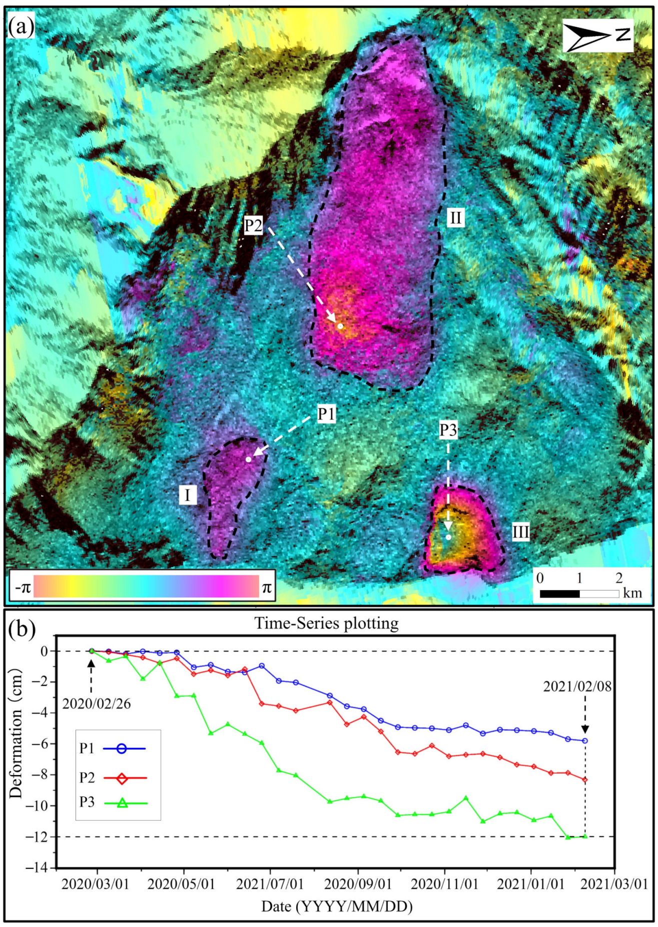


**Figure 3.** Time series InSAR displacement distribution of the Niexia slope: (**a**) cumulative displacement obtained by the Stacking-InSAR technique; (**b**) time series displacement of P1, P2, and P3.

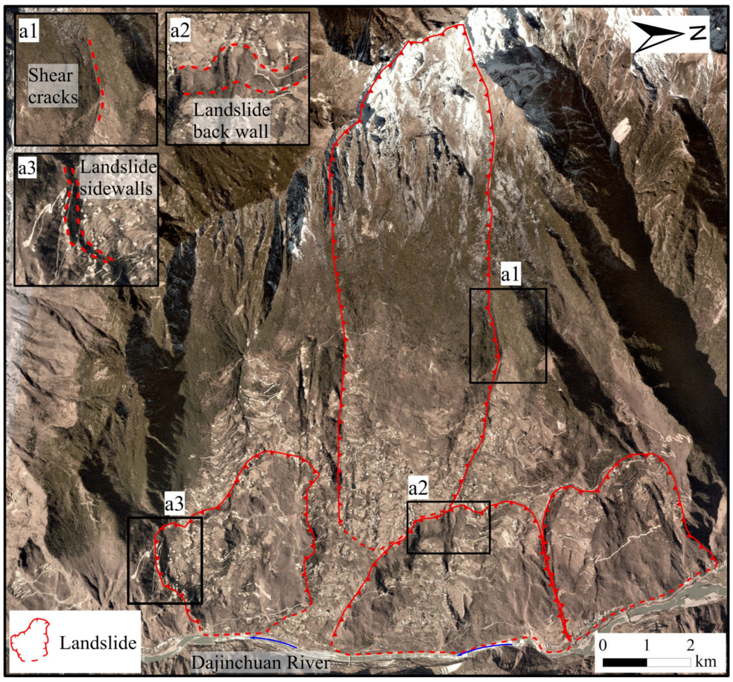


**Figure 4.** Micro-geomorphology identification of sub landslides from optical remote sensing based on: (**a1**) shear cracks (**a2**); landslide back wall; (**a3**) landslide sidewalls.

The vegetation coverage in high mountain and valley areas is dense, and LiDAR technology can obtain DEM that reflects realistic geomorphic features because of its good vegetation penetration ability. Potential landslide boundary interpretation can be performed for landslide micro-geomorphology such as landslide walls, trailing edge cracks, landslide terraces, loose accumulations, and landslide shear cracks left on the surface after historical displacement damage [25,29,60]. The recognition result is shown in Figure 5, and the landslide micro-geomorphic features are clearly visible on the DEM after the removal of vegetation; landslide sidewalls as shown in a1, shear cracks as shown in a2, and trailing edge cracks as shown in a3. From the detailed view shown in the a3 area, it is obvious that the loose accumulation left in the lower half of the trailing edge cracks can be seen; based on these landslide micro-geomorphologies, nine landslides are identified overall through visual interpretation.

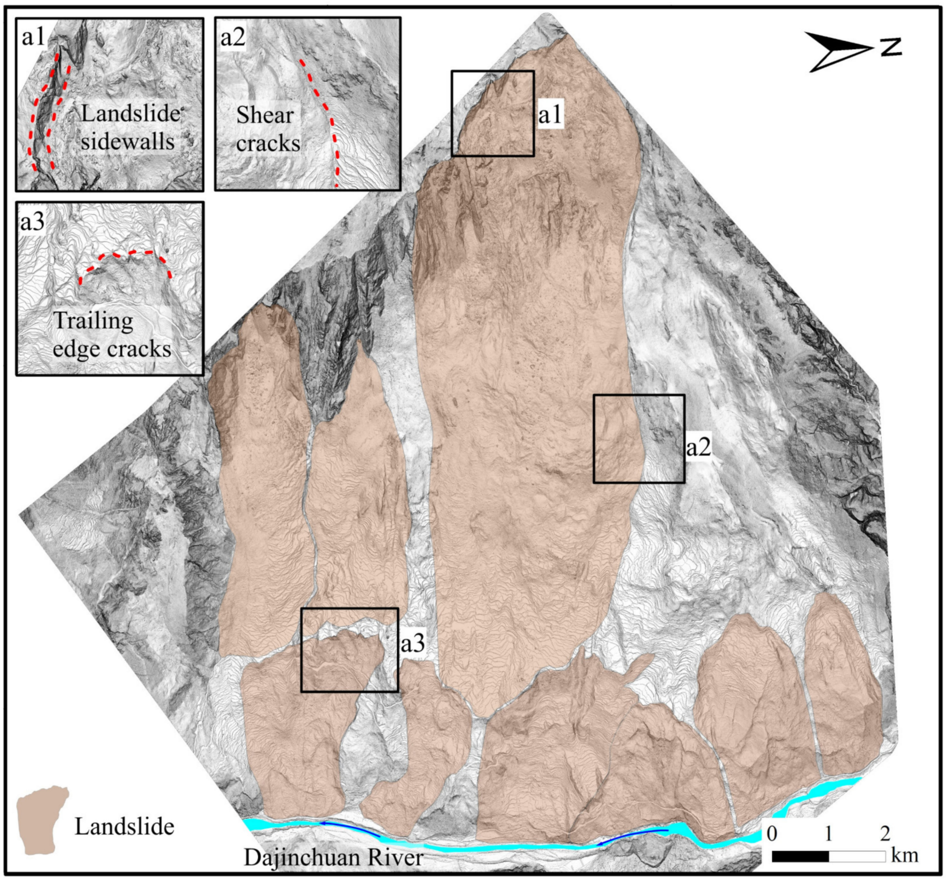


**Figure 5.** Micro-geomorphic identification of sub-landslides based on SVF: (**a1**) Landslide sidewalls, (**a2**) shear cracks, (**a3**) trailing edge cracks.

## 5. Discussion

### *5.1. Comparative Analysis of Multi-Source Remote Sensing Results*

Overlaying the recognition results of the above three techniques on SVF (Figure 6), the black dashed line is the active landslide boundary identified by InSAR technology, the light brown surface is the landslide boundary interpreted by LiDAR technology, and the red line segment is the landslide boundary interpreted by optical image. As can be seen from Figure 6, InSAR technology identified three landslides, while LiDAR technology identified nine landslides, and optical imaging identified four landslides; the three technologies together identified three same landslides. By combining the results, it is inferred that the main reason for this discrepancy is caused by the different advantages and disadvantages of InSAR, LiDAR, and optical remote sensing technologies in landslide identification, interpretation standards, and the situations in which they are applied. Among them, the

InSAR technology is mainly used for landslide identification and boundary determination by the displacement magnitude of the landslide body. However, optical remote sensing images and DEM with real micro-geomorphic features obtained by LiDAR technology are based on landslide micro-geomorphology for potential landslide boundary interpretation. Therefore, for some landslides in areas with dense vegetation cover and some ancient landslides where the original geomorphology has changed due to natural and man-made factors, it is difficult to interpret the boundaries of potential landslides with an optical image, while LiDAR technology can reduce the influence of these factors to a great extent due to its good vegetation penetration ability, so the number and boundaries of the interpretation results of the two technologies may also be different.

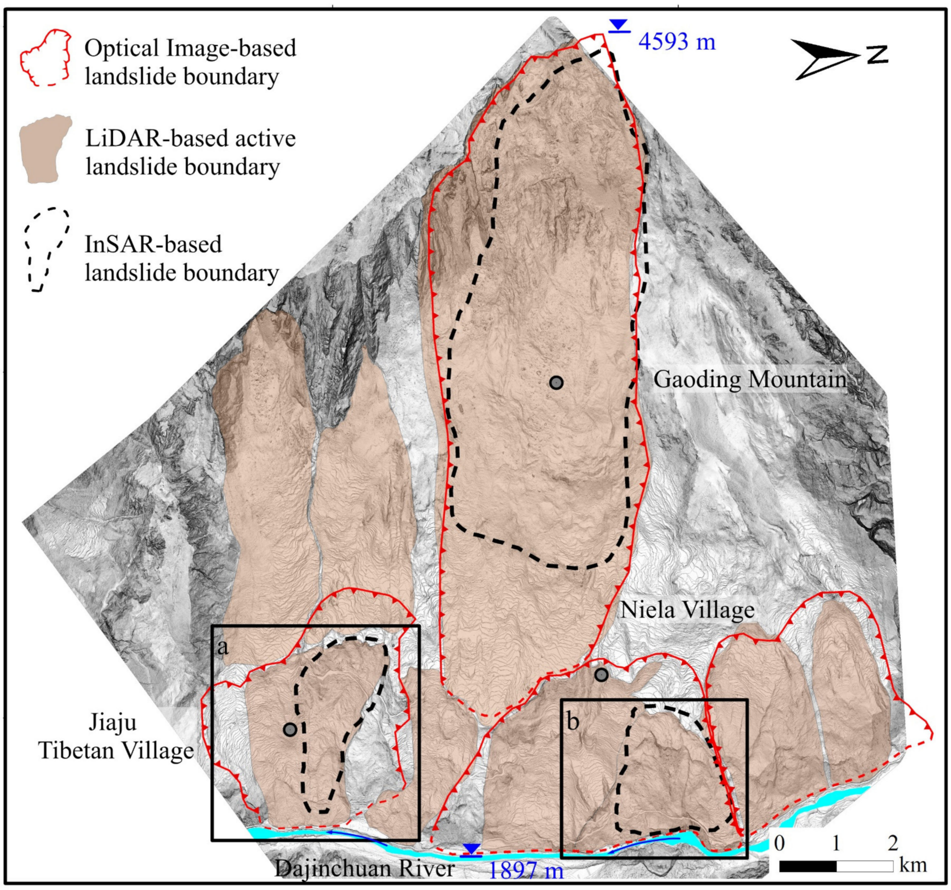


**Figure 6.** Comparison of identification boundaries from three technologies: (**a**,**b**) were selected for detailed comparison.

In addition, the details of the three technologies at the landslide boundary interpretation are shown with two of the typical areas as examples. As shown in Figure 7, in the same area, the InSAR technology recognition result graph is not reflected in the geomorphic features of the landslide, but more in the reflection of the landslide displacement area and the magnitude of the displacement. Landslide geomorphic features such as landslide trailing edge cracks, secondary sliding, and landslide sidewalls can be clearly seen on the SVF from Figure 7(a3,b3), which the optical image cannot represent. As can be seen in Figure 7(a3,b3), the SVF has clear geomorphic features, such as landslide sidewalls, landslide trailing edge cracks, and secondary sliding formed by historical landslide displacement damage, while the optical image is not as intuitive and clear in the representation of these features as the SVF. Therefore, LiDAR technology undoubtedly has more advantages in the interpretation of potential landslide boundaries, and the interpreted boundaries are more detailed.

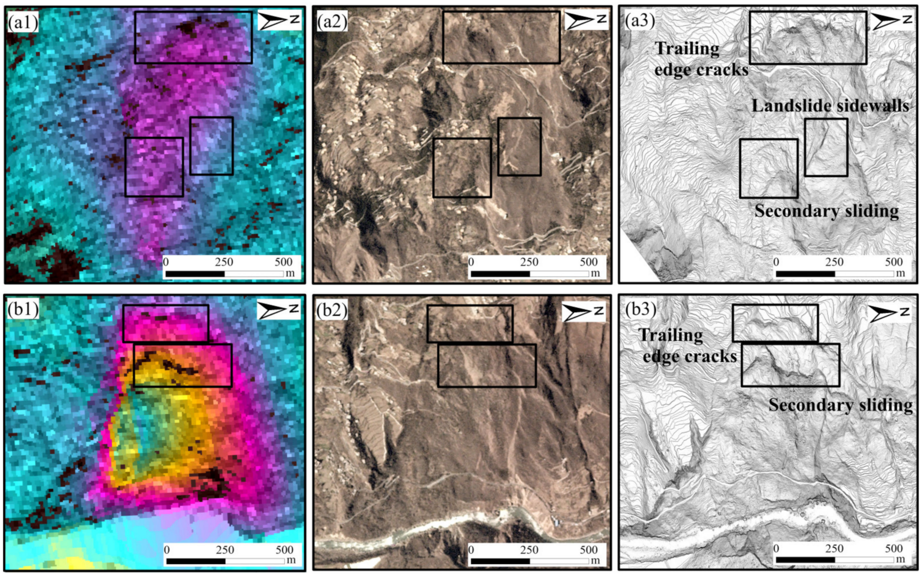


**Figure 7.** Detailed comparison of the three results from the multi-remote sensing technologies: (**a1**,**b1**) is the result of InSAR, (**a2**,**b2**) is the result of optical image sensing, (**a3**,**b3**) is the result of LiDAR.

### 5.2. Comparison of Three Remote Sensing Techniques

From the analysis above, we can see that the three technologies, InSAR, LiDAR, and optical remote sensing, have their own advantages and disadvantages, and they are different in terms of monitoring objects. InSAR technology can monitor small displacements, which has the advantages of high monitoring accuracy, wide monitoring range, independence of weather, and time series analysis ability. However, InSAR technology cannot identify landslides with no signs of displacement and cannot reflect landslide micro-geomorphology. Optical remote sensing images mainly monitor the ongoing displacement area and historical displacement area and have the advantages of a wide monitoring range, reflecting the micro-geomorphology of landslides, and allowing analysis of the spatial and temporal evolution of landslides, but they are easily affected by vegetation, human engineering, and cloudy weather. The main monitoring object of LiDAR technology is the historical displacement area. It has the advantages of not being affected by vegetation and reflecting landslide micro-geomorphology. However, the acquisition cost of this technology is high, and it is difficult to perform large-scale landslide identification (Table 2).

**Table 2.** Advantages and disadvantages of the three remote sensing techniques and monitoring objects.

| Methodology | Monitoring Objects | Advantages | Disadvantages |
|---|---|---|---|
| InSAR | The ongoing displacement area | All-day, all-weather, wide coverage, high accuracy, monitor small displacement, can identify landslides based on the level of displacement, and conduct time series analysis | Cannot identify landslides with no signs of displacement, cannot reflect landslide micro-geomorphology |
| Optical Image | The ongoing displacement area, the historical displacement area | Wide coverage, landslide identification based on landslide micro-geomorphology, spatial and temporal evolution analysis | Easily affected by vegetation, human engineering, and cloudy weather |
| LiDAR | The historical displacement area | Removing the influence of vegetation and obtaining DEM with realistic geomorphic features | High cost and difficult to identify landslides on a large scale |

The three techniques have advantages and disadvantages in terms of monitoring objects, monitoring range, and monitoring accuracy. The integration of the three techniques is certainly more comprehensive for potential landslide identification on high and steep slopes with dense vegetation cover.

## 6. Conclusions

The Niexia slope is located in the alpine valley area. It is difficult for a single remote sensing technology to identify this potential landslide with dense vegetation cover and on steep slopes. In this study, InSAR technology, LiDAR technology, and optical remote sensing images have been used to identify the landslides of the Niexia slope. Based on the different measuring objects, InSAR technology identified three potential landslides, optical remote sensing image identified four potential landslides, and LiDAR technology identified nine potential landslides. Finally, the identification results of the three technologies were combined and analyzed. The results show that the combination of three remote sensing techniques can further improve the comprehensiveness of potential landslide identification on the Niexia slope.

InSAR technology has the advantages of all-weather and all-day, ability to identify the area that is being deformed, and up to millimeter-level accuracy. However, it cannot effectively identify landslides without obvious signs of displacement. Optical remote sensing images have the advantages of wide coverage, reflecting the landslide micro-geomorphology, and analyzing the spatial and temporal evolution of landslides. However, for areas with dense vegetation cover and seriously affected by cloud weather and human activities, the quality of optical images will be seriously affected. Because LiDAR technology has the ability of good vegetation penetration, it can effectively obtain DEM that can reflect the realistic geomorphic features. However, the acquisition of LiDAR data requires a lot of time and money, so it is difficult to apply to large-scale landslide identification. The three technologies have their own advantages and disadvantages. The combination of these three technologies to identify potential landslides on high and steep slopes will be more comprehensive. This study provides an important case for future landslide identification.

**Author Contributions:** Data curation, T.Y.; investigation, Z.L.; methodology, X.D. and K.D.; project administration, X.D.; supervision, Q.X.; validation, B.Y.; visualization, G.Z.; writing—original draft, T.Y.; writing—review and editing, K.D. and S.P. All authors have read and agreed to the published version of the manuscript.

**Funding:** This research was funded by the National Natural Science Foundation of China Major Program (41941019), the fellowship of China Postdoctoral Science Foundation (2020M673322), National Key Research and Development Program of China (2021YFB3901403), Open Research Fund Program of MNR Key Laboratory for Geo-Environmental Monitoring of Great Bay Area: (20220006); the State Key Laboratory of Geohazard Prevention and Geoenvironment Protection Independent Research Project (SKLGP2020Z012).

**Conflicts of Interest:** The authors declare no conflict of interest.

## References

1. Petley, D. Global patterns of loss of life from landslides. *Geology* **2012**, *40*, 927–930. [CrossRef]
2. Froude, M.J.; Petley, D.N. Global fatal landslide occurrence from 2004 to 2016. *Nat. Hazards Earth Syst. Sci.* **2018**, *18*, 2161–2181. [CrossRef]
3. Marcelino, E.V.; Formaggio, A.R.; Maeda, E.E. Landslide inventory using image fusion techniques in brazil. *Int. J. Appl. Earth Obs. Geoinf.* **2009**, *11*, 181–191. [CrossRef]
4. Dai, K.; Xu, Q.; Li, Z.; Tomás, R.; Fan, X.; Dong, X.; Li, W.; Zhou, Z.; Gou, J.; Ran, P. Post-disaster assessment of 2017 catastrophic Xinmo landslide (China) by spaceborne SAR interferometry. *Landslides* **2019**, *16*, 1189–1199. [CrossRef]
5. Xia, Z.; Motagh, M.; Li, T.; Roessner, S. The June 2020 Aniangzhai landslide in Sichuan Province, Southwest China: Slope instability analysis from radar and optical satellite remote sensing data. *Landslides* **2022**, *19*, 313–329. [CrossRef]
6. Singh, A.; Adaphro, A.; Niraj, K.; Dubey, C.; Shukla, D.P. Analysing the causes and lessons learned from Tupul Landslide, Noney district, Manipur. *Res. Sq.* **2022**, preprint. [CrossRef]
7. Solari, L.; Del Soldato, M.; Raspini, F.; Barra, A.; Bianchini, S.; Confuorto, P.; Casagli, N.; Crosetto, M. Review of satellite interferometry for landslide detection in italy. *Remote Sens.* **2020**, *12*, 1351. [CrossRef]

8. Li, X.E.; Zhou, L.; Su, F.Z.; Wu, W.Z. Application of insar technology in landslide hazard: Progress and prospects. *Natl. Remote Sens. Bull.* **2021**, *25*, 614–629.
9. Xie, M.; Huang, J.; Wang, L.; Huang, J.; Wang, Z. Early landslide detection based on D-InSAR technique at the Wudongde hydropower reservoir. *Environ. Earth Sci.* **2016**, *75*, 717. [CrossRef]
10. Zhang, Y.; Meng, X.; Jordan, C.; Novellino, A.; Dijkstra, T.; Chen, G. Investigating slow-moving landslides in the Zhouqu region of China using InSAR time series. *Landslides* **2018**, *15*, 1299–1315. [CrossRef]
11. Zhao, C.; Kang, Y.; Zhang, Q.; Lu, Z.; Li, B. Landslide identification and monitoring along the Jinsha River catchment (Wudongde reservoir area), China, using the InSAR method. *Remote Sens.* **2018**, *10*, 993. [CrossRef]
12. Guo, R.; Li, S.; Chen, Y.n.; Li, X.; Yuan, L. Identification and monitoring landslides in Longitudinal Range-Gorge Region with InSAR fusion integrated visibility analysis. *Landslides* **2021**, *18*, 551–568. [CrossRef]
13. Liu, Z.; Qiu, H.; Zhu, Y.; Liu, Y.; Yang, D.; Ma, S.; Zhang, J.; Wang, Y.; Wang, L.; Tang, B. Efficient Identification and Monitoring of Landslides by Time-Series InSAR Combining Single-and Multi-Look Phases. *Remote Sens.* **2022**, *14*, 1026. [CrossRef]
14. Ren, T.; Gong, W.; Gao, L.; Zhao, F.; Cheng, Z. An Interpretation Approach of Ascending–Descending SAR Data for Landslide Identification. *Remote Sens.* **2022**, *14*, 1299. [CrossRef]
15. Dai, K.; Deng, J.; Xu, Q.; Li, Z.; Shi, X.; Hancock, C.; Wen, N.; Zhang, L.; Zhuo, G. Interpretation and sensitivity analysis of the InSAR line of sight displacements in landslide measurements. *GIScience Remote Sens.* **2022**, *59*, 1226–1242. [CrossRef]
16. Dai, K.; Li, Z.; Tomás, R.; Liu, G.; Yu, B.; Wang, X.; Cheng, H.; Chen, J.; Stockamp, J. Monitoring activity at the daguangbao mega-landslide (China) using sentinel-1 tops time series interferometry. *Remote Sens. Environ.* **2016**, *186*, 501–513. [CrossRef]
17. Dai, K.; Li, Z.; Xu, Q.; Bürgmann, R.; Milledge, D.G.; Tomas, R.; Fan, X.; Zhao, C.; Liu, X.; Peng, J. Entering the era of earth observation-based landslide warning systems: A novel and exciting framework. *IEEE Geosci. Remote Sens. Mag.* **2020**, *8*, 136–153. [CrossRef]
18. Wen, N.; Zeng, F.; Dai, K.; Li, T.; Zhang, X.; Pirasteh, S.; Liu, C.; Xu, Q. Evaluating and Analyzing the Potential of the Gaofen-3 SAR Satellite for Landslide Monitoring. *Remote Sens.* **2022**, *14*, 4425. [CrossRef]
19. Pourkhosravani, M.; Mehrabi, A.; Pirasteh, S.; Derakhshani, R. Monitoring of maskun landslide and determining its quantitative relationship to different climatic conditions using D-InSAR and PSI techniques. *Geomat. Nat. Hazards Risk* **2022**, *13*, 1134–1153. [CrossRef]
20. Dai, K.; Yongbo, T.; Qiang, X.; Ye, F.; Guanchen, Z.; Xianlin, S. Early identification of potential landslide geohazards in alpine-canyon terrain based on SAR interferometry—A case study of the middle section of Yalong river. *J. Radars* **2020**, *9*, 554–568.
21. Eeckhaut, M.V.D.; Poesen, J.; Verstraeten, G.; Vanacker, V.; Nyssen, J.; Moeyersons, J.; Beek, L.v.; Vandekerckhove, L. Use of LIDAR-derived images for mapping old landslides under forest. *Earth Surf. Process. Landf.* **2007**, *32*, 754–769. [CrossRef]
22. Bernat Gazibara, S.; Krkač, M.; Mihalić Arbanas, S. Landslide inventory mapping using LiDAR data in the City of Zagreb (Croatia). *J. Maps* **2019**, *15*, 773–779. [CrossRef]
23. Pirasteh, S.; Li, J. Developing an algorithm for automated geometric analysis and classification of landslides incorporating LiDAR-derived DEM. *Environ. Earth Sci.* **2018**, *77*, 414. [CrossRef]
24. Görüm, T. Landslide recognition and mapping in a mixed forest environment from airborne LiDAR data. *Eng. Geol.* **2019**, *258*, 105155. [CrossRef]
25. Bostjančić, I.; Filipović, M.; Gulam, V.; Pollak, D. Regional-scale landslide susceptibility mapping using limited LiDAR-based landslide inventories for Sisak-Moslavina County, Croatia. *Sustainability* **2021**, *13*, 4543. [CrossRef]
26. Kasai, M.; Ikeda, M.; Asahina, T.; Fujisawa, K. LiDAR-derived DEM evaluation of deep-seated landslides in a steep and rocky region of Japan. *Geomorphology* **2009**, *113*, 57–69. [CrossRef]
27. Guo, C.; Xu, Q.; Dong, X.; Liu, X.; She, J. Geohazard recognition by airborne LiDAR technology in complex mountain areas. *Geomat. Inf. Sci. Wuhan Univ.* **2021**, *46*, 1538–1547.
28. Wang, G.; Joyce, J.; Phillips, D.; Shrestha, R.; Carter, W. Delineating and defining the boundaries of an active landslide in the rainforest of puerto rico using a combination of airborne and terrestrial LiDAR data. *Landslides* **2013**, *10*, 503–513. [CrossRef]
29. Gaidzik, K.; Ramírez-Herrera, M.T.; Bunn, M.; Leshchinsky, B.A.; Olsen, M.; Regmi, N.R. Landslide manual and automated inventories, and susceptibility mapping using LiDAR in the forested mountains of Guerrero, Mexico. *Geomat. Nat. Hazards Risk* **2017**, *8*, 1054–1079. [CrossRef]
30. Shi, W.; Deng, S.; Xu, W. Extraction of multi-scale landslide morphological features based on local Gi* using airborne LiDAR-derived DEM. *Geomorphology* **2018**, *303*, 229–242. [CrossRef]
31. Bunn, M.D.; Leshchinsky, B.A.; Olsen, M.J.; Booth, A. A simplified, object-based framework for efficient landslide inventorying using LiDAR digital elevation model derivatives. *Remote Sens.* **2019**, *11*, 303. [CrossRef]
32. Pirasteh, S.; Li, J. Landslides investigations from geoinformatics perspective: Quality, challenges, and recommendations. *Geomat. Nat. Hazards Risk* **2017**, *8*, 448–465. [CrossRef]
33. Ouyang, C.; Zhao, W.; Xu, Q.; Peng, D.; Li, W.; Wang, D.; Zhou, S.; Hou, S. Failure mechanisms and characteristics of the 2016 catastrophic rockslide at Su village, Lishui, China. *Landslides* **2018**, *15*, 1391–1400. [CrossRef]
34. Yang, W.; Wang, Y.; Wang, Y.; Ma, C.; Ma, Y. Retrospective deformation of the Baige landslide using optical remote sensing images. *Landslides* **2020**, *17*, 659–668. [CrossRef]
35. Qu, F.; Qiu, H.; Sun, H.; Tang, M. Post-failure landslide change detection and analysis using optical satellite Sentinel-2 images. *Landslides* **2021**, *18*, 447–455. [CrossRef]

36. Liu, R.; Li, L.; Pirasteh, S.; Lai, Z.; Yang, X.; Shahabi, H. The performance quality of LR, SVM, and RF for earthquake-induced landslides susceptibility mapping incorporating remote sensing imagery. *Arab. J. Geosci.* **2021**, *14*, 259. [CrossRef]
37. Ye, C.; Li, Y.; Cui, P.; Liang, L.; Pirasteh, S.; Marcato, J.; Gonçalves, W.N.; Li, J. Landslide detection of hyperspectral remote sensing data based on deep learning with constrains. *IEEE J. Sel. Top. Appl. Earth Obs. Remote Sens.* **2019**, *12*, 5047–5060. [CrossRef]
38. Gao, J.; Maro, J. Topographic controls on evolution of shallow landslides in pastoral Wairarapa, New Zealand, 1979–2003. *Geomorphology* **2010**, *114*, 373–381. [CrossRef]
39. Li, W.; Xu, Q.; Lu, H.; Dong, X.; Zhu, Y. Tracking the deformation history of large-scale rocky landslides and its enlightenment. *Geomat. Inf. Sci. Wuhan Univ.* **2019**, *44*, 1043–1053.
40. Fiorucci, F.; Giordan, D.; Santangelo, M.; Dutto, F.; Rossi, M.; Guzzetti, F. Criteria for the optimal selection of remote sensing optical images to map event landslides. *Nat. Hazards Earth Syst. Sci.* **2018**, *18*, 405–417. [CrossRef]
41. Wang, Z.; Zhao, C.; Liu, X.; Li, B. Evolution analysis and deformation monitoring of Yigong landslide in Tibet with optical remote sensing and InSAR. *J. Wuhan Univ. Inf. Sci. Ed.* **2021**, *46*, 1569Y–1578Y.
42. Guo, X.; Guo, Q.; Feng, Z. Detecting the vegetation change related to the creep of 2018 Baige landslide in Jinsha river, SE Tibet using spot data. *Front. Earth Sci.* **2021**, *9*, 706998. [CrossRef]
43. Yin, Y.; Zheng, W.; Liu, Y.; Zhang, J.; Li, X. Integration of GPS with InSAR to monitoring of the Jiaju landslide in Sichuan, China. *Landslides* **2010**, *7*, 359–365. [CrossRef]
44. Dong, J.; Zhang, L.; Tang, M.; Liao, M.; Xu, Q.; Gong, J.; Ao, M. Mapping landslide surface displacements with time series SAR interferometry by combining persistent and distributed scatterers: A case study of Jiaju landslide in Danba, China. *Remote Sens. Environ.* **2018**, *205*, 180–198. [CrossRef]
45. Ao, M.; Zhang, L.; Shi, X.; Liao, M.; Dong, J. Measurement of the three-dimensional surface deformation of the Jiaju landslide using a surface-parallel flow model. *Remote Sens. Lett.* **2019**, *10*, 776–785. [CrossRef]
46. Xu, Q.; Dong, X.; Li, W. Integrated Space-Air-Ground Early Detection, Monitoring and Warning System for Potential Catastrophic Geohazards. *Geomat. Inf. Sci. Wuhan Univ.* **2019**, *44*, 957–966.
47. Xu, Q. Understanding and Consideration of Related issues in Early Identification of Potential Geohazards. *Geomat. Inf. Sci. Wuhan Univ.* **2020**, *45*, 1651–1659.
48. Xu, Q.; Guo, C.; Dong, X.; Li, W.; Lu, H.; Fu, H.; Liu, X. Mapping and characterizing displacements of landslides with InSAR and airborne LiDAR technologies: A case study of danba county, southwest China. *Remote Sens.* **2021**, *13*, 4234. [CrossRef]
49. Farr, T.G.; Rosen, P.A.; Caro, E.; Crippen, R.; Duren, R.; Hensley, S.; Kobrick, M.; Paller, M.; Rodriguez, E.; Roth, L. The shuttle radar topography mission. *Rev. Geophys.* **2007**, *45*, RG2004. [CrossRef]
50. Conrad, O.; Bechtel, B.; Bock, M.; Dietrich, H.; Fischer, E.; Gerlitz, L.; Wehberg, J.; Wichmann, V.; Böhner, J. System for automated geoscientific analyses (SAGA) v. 2.1. 4. *Geosci. Model Dev.* **2015**, *8*, 1991–2007. [CrossRef]
51. Lo, C.-M.; Lee, C.-F.; Keck, J. Application of sky view factor technique to the interpretation and reactivation assessment of landslide activity. *Environ. Earth Sci.* **2017**, *76*, 375. [CrossRef]
52. Costantini, M. A novel phase unwrapping method based on network programming. *IEEE Trans. Geosci. Remote Sens.* **1998**, *36*, 813–821. [CrossRef]
53. Goldstein, R.M.; Werner, C.L. Radar interferogram filtering for geophysical applications. *Geophys. Res. Lett.* **1998**, *25*, 4035–4038. [CrossRef]
54. Hooper, A.; Zebker, H.A. Phase unwrapping in three dimensions with application to InSAR time series. *JOSA A* **2007**, *24*, 2737–2747. [CrossRef] [PubMed]
55. Soltanieh, A.; Macciotta, R. Updated understanding of the Ripley landslide kinematics using satellite InSAR. *Geosciences* **2022**, *12*, 298. [CrossRef]
56. Jones, N.; Manconi, A.; Strom, A. Active landslides in the Rogun Catchment, Tajikistan, and their river damming hazard potential. *Landslides* **2021**, *18*, 3599–3613. [CrossRef]
57. Piroton, V.; Schlögel, R.; Barbier, C.; Havenith, H.-B. Monitoring the recent activity of landslides in the Mailuu-Suu Valley (Kyrgyzstan) using radar and optical remote sensing techniques. *Geosciences* **2020**, *10*, 164. [CrossRef]
58. Xiao, R.; Yu, C.; Li, Z.; Jiang, M.; He, X. Insar stacking with atmospheric correction for rapid geohazard detection: Applications to ground subsidence and landslides in China. *Int. J. Appl. Earth Obs. Geoinf.* **2022**, *115*, 103082. [CrossRef]
59. Fiorucci, F.; Cardinali, M.; Carlà, R.; Rossi, M.; Mondini, A.; Santurri, L.; Ardizzone, F.; Guzzetti, F. Seasonal landslide mapping and estimation of landslide mobilization rates using aerial and satellite images. *Geomorphology* **2011**, *129*, 59–70. [CrossRef]
60. Glenn, N.F.; Streutker, D.R.; Chadwick, D.J.; Thackray, G.D.; Dorsch, S.J. Analysis of LiDAR-derived topographic information for characterizing and differentiating landslide morphology and activity. *Geomorphology* **2006**, *73*, 131–148. [CrossRef]
61. Kang, Y.; Zhao, C.; Zhang, Q.; Lu, Z.; Li, B. Application of InSAR techniques to an analysis of the Guanling landslide. *Remote Sens.* **2017**, *9*, 1046. [CrossRef]
62. Chen, L.; Zhao, C.; Li, B.; He, K.; Ren, C.; Liu, X.; Liu, D. Deformation monitoring and failure mode research of mining-induced Jianshanying landslide in karst mountain area, China with ALOS/PALSAR-2 images. *Landslides* **2021**, *18*, 2739–2750. [CrossRef]
63. Zhang, L.; Dai, K.; Deng, J.; Ge, D.; Liang, R.; Li, W.; Xu, Q. Identifying potential landslides by stacking-InSAR in southwestern China and its performance comparison with SBAS-InSAR. *Remote Sens.* **2021**, *13*, 3662. [CrossRef]